Patient-based 4D digital breast phantom for perfusion contrast-enhanced breast CT imaging

Marco Caballo and Ritse Mann
Department of Radiology and Nuclear Medicine, Radboud University Medical Center, PO Box 9101, 6500 HB Nijmegen, The Netherlands

Ioannis Sechopoulos[a)]
Department of Radiology and Nuclear Medicine, Radboud University Medical Center, PO Box 9101, 6500 HB Nijmegen, The Netherlands
Dutch Expert Center for Screening (LRCB), PO Box 6873, 6503 GJ Nijmegen, The Netherlands

Purpose: The purpose of this study was to develop a realistic patient-based 4D digital breast phantom including time-varying contrast enhancement for simulation of dedicated breast CT perfusion imaging.

Methods: A 3D static phantom is first created by segmenting a breast CT image from a healthy patient into skin, fibroglandular tissue, adipose tissue, and vasculature. For the creation of abnormal cases, a breast lesion model was developed and can be added to the phantom. After defining the necessary perfusion parameters for each tissue (e.g., arterial input function for vasculature, blood volume and blood flow for the other normal tissues) based on contrast-enhanced dynamic breast MRI data, the corresponding time-enhancement curves are computed for each voxel in the phantom, according to tissue type. These curves are calculated by convolution between the arterial input function and a shifted exponential function. This exponential depends on the perfusion parameters associated with each tissue voxel, and, to incorporate normal biological variability, a uniform random distribution is used to vary the perfusion parameters on a voxel-basis. Finally, a 4D array is produced by sampling the continuous time-enhancement curves at the desired sampling rate. Beside modeling different enhancement dynamics according to the given input perfusion parameters, the phantom also includes the possibility to realistically simulate different spatial enhancement patterns for the breast parenchyma, taking into account the arterial sources supplying the breast. Finally, different patterns of contrast medium uptake can also be simulated for the tumor models (homogeneous and rim enhancement).

Results: As an example, a typical 4D phantom has dimensions of $426 \times 421 \times 260 \times 559$ (x, y, z, t), with a voxel size of 273 μm and a sampling time of 1 s. The characteristics of the tumor model can be modified at will to evaluate perfusion in different types of breast lesions. Results show the expected enhancement of tissues, consistent with the given input parameters. Moreover, the tumor models evaluated in this work show different enhancement dynamics according to the tumor type (defined by different input perfusion parameters), and also present a higher enhancement compared to the other healthy tissues, as expected.

Conclusions: The proposed digital phantom can model the breast tissue perfusion during 4D breast CT image acquisition, displaying the different enhancement dynamics that could be found in a real patient breast. This phantom can be used during the development of dynamic contrast-enhanced dedicated breast CT imaging, for optimization of image acquisition, image reconstruction, and image analysis. This modality could provide functional information of the breast, resulting in detection, diagnosis, and treatment improvements of breast cancer with breast CT. © *2018 The Authors. Medical Physics published by Wiley Periodicals, Inc. on behalf of American Association of Physicists in Medicine.* [https://doi.org/10.1002/mp.13156]

1. INTRODUCTION

Breast cancer is still the most common cause of female cancer death in Europe.[1] Although mammographic screening and improvements in treatment have reduced breast cancer mortality by 30%,[2] this disease still causes half a million deaths per year worldwide.[3]

In current years, there has been strong development in imaging techniques to improve early detection and staging of breast cancer. Digital breast tomosynthesis (DBT), an imaging method that produces pseudo–three-dimensional images of the breast from multiple 2D projections over a limited angular range,[4] is first among the improvements in x ray-based techniques and is currently widely implemented in clinical practice. Although resulting in improved performance in breast cancer detection,[5] DBT is not a fully 3D technique, since the angular range covered during acquisition is limited. Dedicated breast computed tomography (breast CT) has been

introduced to overcome this limitation. Breast CT is a fully 3D, isotropic, high spatial and contrast resolution x ray-based modality which brings the characteristics of tomography to breast imaging.[6] Given these advantages, breast CT has the potential for being used in multiple breast imaging applications, such as detection, diagnosis, staging, and therapy response monitoring.

However, clinical performance based upon anatomic evaluation alone is limited due to the similar attenuation of normal fibroglandular and cancerous tissue. Functional information can be acquired via noninvasive imaging by use of a contrast medium and evaluation of its uptake within a patient breast, and in eventual lesions. For both dynamic contrast-enhancement MRI (DCE-MRI) and contrast-enhanced spectral mammography (CESM), it has been shown that the administration of contrast increases the sensitivity up to 98%.[7] Dynamic uptake information is also extremely valuable for lesion classification, reducing the need for biopsies of benign lesions.

Dynamic contrast-enhanced dedicated breast CT (DCE-breast CT)[8] may, therefore, be used in a manner similar to DCE-MRI: acquiring multiple images over time prior to and after the injection of iodinated contrast medium.[9,10] Given that a complete breast CT acquisition can currently be achieved in 10 s, and that spatial resolution is independent of scan time, DCE-breast CT could achieve a higher combined spatial and temporal resolution than DCE-MRI, with the potential advantage of improving tumor diagnosis and characterization even further.

In breast CT, the voxel values are linearly proportional to attenuation. Therefore, an iodinated contrast agent may be useful for quantifying the capillary permeability differences between normal and malignant tissues, which is easier than in MRI since the signal intensity changes induced by the contrast agent are not linearly related to the gadolinium concentration. This quantitation may improve specificity and may allow the use of quantitative enhancement characteristics as imaging biomarker. Furthermore, although DCE-MRI could be used for tumor profiling of intra-tumor heterogeneity to improve diagnosis and staging, it is more prone to several artifacts and is relatively expensive, limiting its use. In addition, it may not achieve a high enough combined spatial/temporal resolution[7] to allow for tumor sub-type characterization at an early stage.

In an attempt to overcome these issues, contrast-enhanced whole-body CT has previously been investigated for breast cancer diagnosis.[11–13] On average, it resulted in a high accuracy (over 95%) and a sensitivity and specificity of 92% and 100%, respectively. Compared to DCE-MRI, especially the high specificity provides clear evidence for the potential of using contrast-enhanced CT in diagnosis, staging and follow-up of breast cancer. However, the lower sensitivity, along with the high delivered radiation dose, limits its use to patients with absolute and relative contraindications to MRI, such as presence of a pacemaker or of clips, claustrophobia, and severe dyspnea due to heart disease.[11] The major limitations of whole-body CT for breast imaging, especially the

relatively low spatial resolution and high dose (also outside of the breasts) are addressed with the development of contrast-enhanced dedicated breast CT. In addition, breast CT uses a significantly lower energy when compared to whole-body CT, thus resulting in increased soft tissue contrast. These advantages may result in an increase in the sensitivity of DCE-breast CT compared to body CT, while maintaining the high specificity due to the sharing of the physics of the imaging process and the kinetics of the contrast agent.

For further development and optimization of DCE-breast CT, tools are needed to simulate the DCE-breast CT imaging process. As a first step, a realistic phantom able to mimic the perfusion process observed in breast tissue, breast blood vessels, and breast tumors is needed to recreate the dynamic image acquisition process. Such a phantom could be used in computer simulations of DCE-breast CT imaging for testing and optimization of image acquisition, reconstruction, and processing algorithms, as well as validating new automated image analysis methods to extract quantitative biomarker information from the DCE-breast CT images.

So far, some approaches have been proposed in literature to design and develop realistic phantoms of different organs and systems of the human body. Previous work has been reported on engineered physical solutions to mimic blood perfusion by contrast agent flow through tissue-like structures.[14–17] These structures adequately simulate soft tissue and allow extensive testing with actual imaging systems, but these phantoms are usually limited in complexity. As an alternative to engineered physical phantoms, a different solution could be to use biological phantoms (i.e., animal models).[18] Although realistic, beside the complexity of their use, these solutions do not allow for investigation of a wide range of physiological conditions, in addition to the rest of the tissue not being representative, in terms of size and complexity, of human tissue.

The use of digital phantoms allows for accurate and more complex anatomical models (compared to physical phantoms) with high repeatability and consistency (compared to animal models) and, importantly, with known ground truth. Digital phantoms can be derived from real patient images, or be completely simulated, and can be easily modified to model different types of pathology or variations in normal anatomy. In addition, simulating images from these phantoms allows complete control over the imaging conditions simulated, including both imaging system characteristics (e.g., acquisition technique, detector specifications) and imaged object characteristics (e.g., motion during and in between scans).[19–22]

Given the realism and the possibility to fully control the object and system parameters that a software phantom can provide, the purpose of this work is therefore to design and develop a realistic patient-based 4D digital breast phantom to simulate breast tissue and tumor perfusion in dynamic contrast-enhanced breast CT imaging. For this, we developed a software tool that, from input patient images acquired with a 3D breast CT system, can generate a 4D phantom with different perfusion features based upon the specification of several

physiological parameters. The method we propose can be used to generate multiple 4D phantoms from the same input image, and allows the modeling of different perfusion patterns and breast lesion models, along with different temporal acquisition settings (i.e., the image acquisition total time range and temporal resolution), covering a variety of scenarios of biological and physical conditions.

2. MATERIALS AND METHODS

All user-selectable parameters for generation of the 4D phantoms are displayed in Tables I and II, and they are detailed in the following subsections. The main pipeline of our method is summarized in Fig. 1 and all steps are described in detail below.

2.A. Image acquisition

Although the algorithm is breast CT system design-independent, the characteristics of the patient images acquired at our institution are given to present a typical example. Patient images were acquired using a clinical breast CT system (Koning Corp., West Henrietta, NY).[23] For this system, the x ray tube with a tungsten target and aluminum filter is set to a voltage of 49 kV, resulting in an x ray spectrum with a 0.3 mm nominal focal spot and a first half value layer of 1.39 mm Al.[24] The detector is 397 × 298 mm in size with 1024 × 768 pixels, (4030CB, Varian Medical Systems, Palo Alto, CA, USA), with a reconstructed voxel size of 273 × 273 × 273 μm. The reconstruction algorithm used is filtered backprojection. The source-to-imager distance of the breast CT system is 92.3 cm, while the source-to-isocenter distance is 65 cm. A complete breast CT scan involves the acquisition of 300 projections over a full 360° revolution of the x ray tube and detector in 10 s. The x ray tube operates in pulsed mode with a constant 8 ms pulse, and the tube current varies from 12 to 100 mA. Images are acquired by trained radiographers, currently as part of an ethics board-approved patient trial on noncontrast-enhanced breast CT, with subjects providing written informed consent.

2.B. Image classification

Since different tissues within the breast show different enhancement rates, it is important to label each voxel of the breast CT image and allocate it to the correct tissue type. For this, a discrete mask was generated, in which each voxel is

TABLE I. Physical input parameters and options for generating the 4D breast phantom, with numerical values adopted in this work.

Parameters	Category	Numerical value adopted in present work
Start time	Temporal parameters	1 (s)
End time		560 (s)
Temporal resolution (sampling time)		1, 10, 20, 30, 60, 90 (s)
Input iodine concentration within the arteries supplying the breast	Contrast medium	10 [mg(I)/ml]
Tumor type flag	Tumor model	Benign/Malignant
Biological variability limits	Biological noise	[−0.5, 0.5]
S_1	Spatial enhancement pattern for breast parenchyma (option)	100 [dimensionless]
t_*		60 (s)
P_i		1/0 and 0.6/0.4
S_2	Rim enhancement (option)	1,000 [dimensionless]

represented by a discrete value, indicating to which tissue type the voxel belongs. Therefore, the first processing step of our pipeline involves the segmentation and classification of breast tissues within the patient 3D breast CT image as adipose tissue, fibroglandular tissue, skin and blood vessels. To address this task, we used an automatic classification algorithm for breast CT image segmentation.[25] Although the breast CT images used in this study are corrected for cupping by the breast CT system during reconstruction, in cases where this correction is not applied, we have shown that the classification algorithm is insensitive to cupping artifacts.[25] Briefly, this algorithm incorporates different unsupervised image analysis techniques to segment each tissue type: constrained region-based segmentation methods for skin detection, an energy minimizing active contour model for adipose tissue classification and a clustering method to detect fibroglandular tissue and blood vessels.

The 3D mask resulting from this algorithm provides a map of all major tissue types within the breast, assigning each voxel of the original image to the correct tissue type and allowing to set the correct perfusion parameters to each tissue, as described later in this section. In Fig. 2, an example of the original 3D breast CT image and the corresponding segmented mask are displayed.

TABLE II. Physiological input parameters for generating the 4D breast phantom, with numerical values adopted in this work (from Delille et al[27]).

	Blood volume $(\overline{BV} \pm V_{BV})$(mL/100 mL)	Blood flow $(\overline{BV} \pm V_{BF})$(mL/min/100 mL)	Mean transit time (*MTT*) [s]	Time to peak (t_{peak}) (s)	Wash-in polynomial grade (R_{washin})	Wash-out polynomial grade ($R_{washout}$)
Fibroglandular tissue	8.5 ± 0.1	7.15 ± 0.1	71.3 ± 1.8	Not defined	Not defined	Not defined
Malignant Lesion model	35.5 ± 0.3	70.3 ± 0.3	30.3 ± 0.4	120	5	3
Benign lesion model	15.4 ± 0.3	14.8 ± 0.3	62.4 ± 2.5	190	1.25	2

2.C. Perfusion input parameters

Once the masked 3D image is obtained, two input parameters related to breast tissue perfusion, the tissue blood volume

FIG. 1. Main steps of the proposed pipeline for the generation of 4D breast phantoms. [Color figure can be viewed at wileyonlinelibrary.com]

(BV) and the tissue blood flow (BF), need to be defined. BV corresponds to the volume of capillary blood contained in a given tissue (expressed in mL of blood/100 mL of tissue),[26] while BF corresponds to the blood flow entering (and exiting) a volume of tissue (expressed in mL of blood/min/100 mL of tissue).[26] Both parameters are useful to compute initial estimates of the contrast medium uptake within a given tissue type; their value can be defined at will, but in this work we used parameter values previously reported in breast DCE-MRI studies,[27] listed in Table II.

Although these two parameters could be defined for each tissue type present in the breast, for ease of computation and to reduce the processing time in generating a phantom, for now they are defined for the fibroglandular tissue only (i.e., adipose tissue and breast skin are considered to have negligible perfusion). From BV and BF, the mean transit time (MTT), which indicates the mean time taken by blood to pass through the tissue capillary network,[26] is defined as follows:

$$MTT = \frac{BV}{BF} \cdot 60 \tag{1}$$

As input to the algorithm, the mean transit time values (expressed in seconds) used in this work are reported in Table II.

Finally, since the quantitative analysis of the microcirculation requires some knowledge of the kinetics of the contrast agent in the afferent artery to the tissue of interest,[28] an average arterial input function (AIF), which describes the enhancement kinetics of the artery supplying the organ, was defined. As well as the other input parameters, the AIF can be varied at will to better define the inter- and intra-variability among different patients and scans. In terms of computation, the AIF is described by 10 points indicating the contrast medium (iodinated solution) concentration within the arteries supplying the breast for a given temporal moment. These points are then interpolated using cubic splines to obtain a final smooth function. Here, we modeled the shape of the AIF (displayed in Fig. 3) according to the work proposed by George et al.[29], in which the AIF was reconstructed from animal models using a
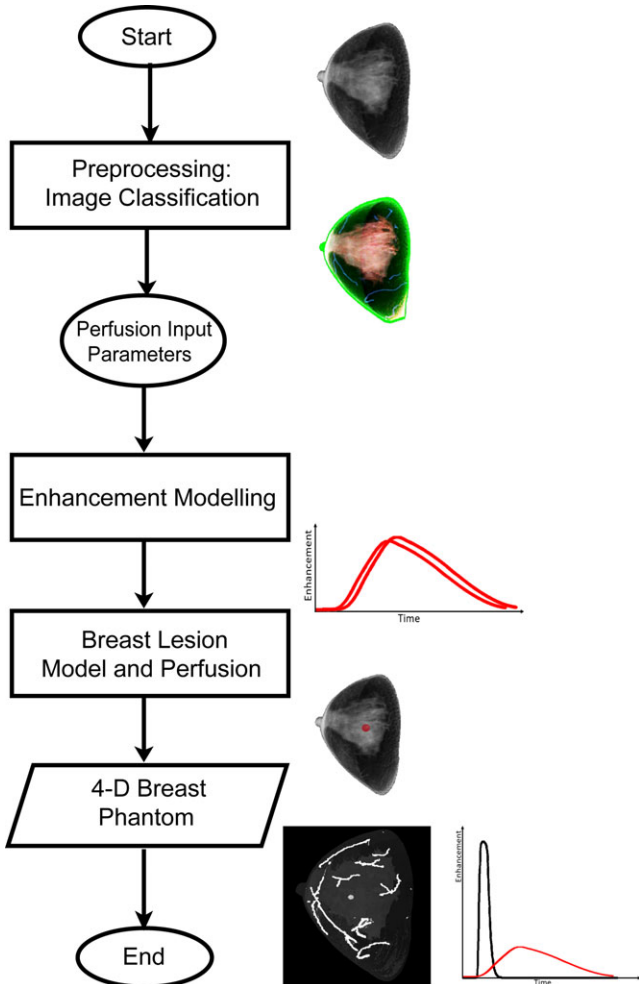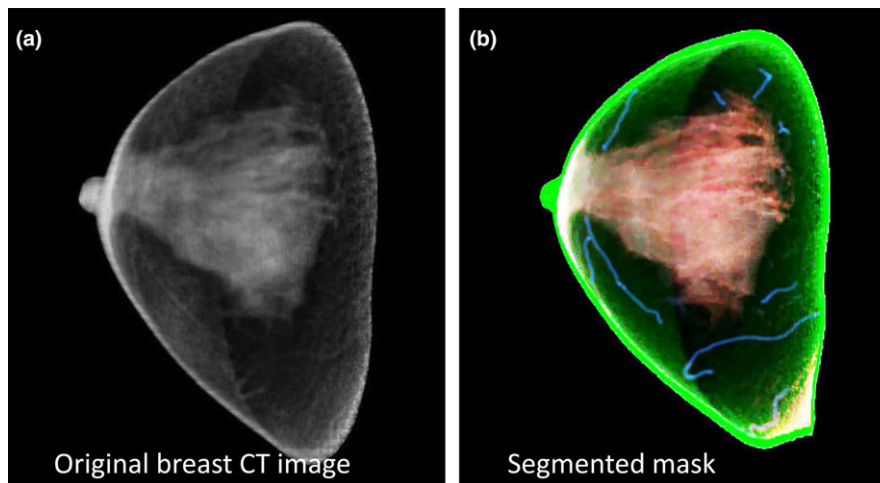

FIG. 2. First step of the 4D breast phantom development algorithm: (a) original 3D BREAST CT image, and (b) the respective 3D segmentation mask, showing skin, blood vessels, fibroglandular tissue, and adipose tissue. Both panels show 3D renderings of a breast CT image (original and segmented) using average intensity projections. [Color figure can be viewed at wileyonlinelibrary.com]
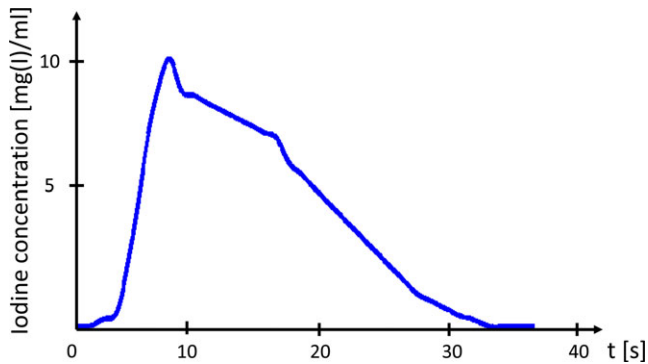
FIG. 3. Arterial input function (AIF) used in this work. [Color figure can be viewed at wileyonlinelibrary.com]

combination of bolus-tracking and time-registered helical multidetector CT data. The amplitude of the curve depends on the contrast medium concentration injected in the breast through its major vasculature, which is another user-selectable parameter. In this work, we set it to 10 mg(I)/mL.[30] The AIF, beside modeling the iodinated solution in- and out-flow within blood vessels, also influences the concentration of iodine in the other breast tissues, as described in the following subsections.

2.D. Enhancement modeling

To introduce expected biological variability among voxels of the same tissue type, the given input perfusion parameters are varied on a voxel-by-voxel basis.

For this, a 3D volume with each voxel labeled with a random number generated from a uniform random distribution normalized between −0.5 and +0.5 is generated, and it is used to vary the perfusion parameters according to the following equation:

$$BV(x, y, z) = \overline{BV} + N(x, y, z) \cdot V_{BV} \qquad (2)$$

$$BF(x, y, z) = \overline{BF} + N(x, y, z) \cdot V_{BF} \qquad (3)$$

where (x, y, z) denote the voxel coordinates within the breast CT image, $\overline{BV}$ and $\overline{BF}$ the average perfusion parameters values, V_{BV} and V_{BF} their variance, and N the random number associated with that voxel. The values for $\overline{BV}$, $\overline{BF}$, V_{BV}, and V_{BF} used for this study are listed in Table II. This operation allows all perfusion parameters to vary in a voxel-by-voxel basis, while still taking into account the variance of the perfusion parameters themselves.

According to the indicator dilution theory,[31] BV and BF can be described by considering a bolus of contrast medium given at time t = 0 in the feeding vessels to a tissue volume of interest (VOI). The contrast medium follows different paths through the VOI, and the resulting transit times have a distribution characteristic for the passage of the medium through the tissue. Therefore, after the injection of the contrast medium inside the patient blood circulation, each tissue within the breast will show a different enhancement, related to the values of BV and BF (and the derived MTT) associated with that tissue. The image enhancement will therefore depend on the amount of blood flowing through the tissue (which mostly determines the magnitude of the enhancement), and on the average time during which the contrast medium concentrates in the tissue interstitium (which mostly determines the duration of the enhancement). To mathematically describe this process, each voxel of the image can be described with a set of different intensity values which represent the time-enhancement curve (TEC) associated with that voxel, which describes the enhancement of the voxel over time. To calculate these curves, the AIF is convolved with a function (which basically models the fraction of contrast medium inside a given tissue) described by the main perfusion parameters used in our model: the amplitude is defined by the BF, while the first moment of the function is set by the MTT (when scaled by the BF, the area under the curve indicates the BV). By convolving this function with the AIF, the latter is reshaped taking into account the BV, BF and MTT values of the tissue, and therefore generating the TEC for a given tissue voxel according to the following equation:

$$TEC(x, y, z, t) = AIF * \begin{cases} BF & if\ t \le MTT \\ BF \cdot e^{-(t-MTT)} & if\ t > MTT \end{cases}$$

$$(4)$$

Finally, to generate more accurate enhancement patterns from a physiological dynamics perspective, we developed a final step to vary the timing of contrast medium uptake within the breast parenchyma modeling the location of major blood vessels supplying the breast. It is expected that some regions of breast tissue may show an earlier enhancement than others, depending on the distance to the major arteries (i.e., the contrast medium will arrive to tissue closer to these major vessels earlier[32]). We therefore implemented a method to model this delay in enhancement in the breast fibroglandular tissue. Although an accurate modeling of this delay should take into account the precise location of the breast arteries endpoints to properly set the spatio-temporal variation in the contrast medium, the impossibility to distinguish, in unenhanced 3D breast CT images, the arteries from the veins limits the feasibility of this approach. In fact, since the enhancement is dependent on the relative distance to the arterial supply, while not so much to the venous drainage, modeling the delay of enhancement according to the distance from breast blood vessels detected with the segmentation algorithm might lead to physiological inaccuracies, since the detected vessels are mostly veins, while the arteries are the only source of contrast medium to the breast fibroglandular tissue. Therefore, we decided to define two input locations to the breast, both in the upper quadrant, on the medial and the lateral side of the input breast CT image. It has been shown that, depending on the patient, the contrast medium can appear from either one or the other of these regions, and in some case from both equally.[33] These points are considered as the locations of the major arteries supplying the breast, and therefore where the contrast medium is more likely to spread from. These points were automatically selected by taking two pixels located at the interior boundary of the breast skin, respectively, chosen

at 45° and 135° on the coronal image slice located closest to the chest wall. After defining these points, the following 3D space was defined:

$$B = \sum_{i=1}^{2} e^{\frac{-\left[(x-x_e(i))^2+(y-y_e(i))^2+(z-z_e(i))^2\right]}{S_1^2}} \cdot P_i \qquad (5)$$

and normalized between 0 and 1. The symbols x_e, y_e, z_e are the spatial coordinates of the two sources of the contrast medium, S_1 is a parameter modeling the spatial distribution of the iodinated solution within the fibroglandular tissue, and P_i represent the biases controlling the percentage of contrast medium between the two source locations (where $\sum_{i=1}^{2} P_i = 1$). These latter parameters (P_1 and P_2) allow to define the amount of iodinated solution coming from each of the two source locations, accounting for the biological variability among different patient cases. For example, an input of 1/0 means that all the enhancement originates from the upper medial corner, a value of 0/1 means all the enhancement comes from the upper lateral corner, 0.5/0.5 means equal enhancement originating from both, and so on.

Local values of function (5) are used to delay, on a voxel-by-voxel basis, the contrast medium uptake within the breast parenchyma according to the distance from these two locations, using the following function:

$$TEC = TEC(t - \left[(1 - B(x,y,z)) \cdot t_*\right]) \qquad (6)$$

where t_* is a parameter modeling the temporal delay of the contrast medium uptake. With this operation, the enhancement of the fibroglandular tissue can be modeled at will by tuning the parameters S_1 (which controls the magnitude of the spatial distribution), t_* (which sets the temporal delay) and P_i (which define the prevalence of the source of contrast). For voxels located close to the source locations, function B will have high values, thus forcing the temporal delay to quasi-zero values. Conversely, most inner parts of the breast tissue will see lower values of B, and therefore, a delayed enhancement. All parameters involved in this model (S_1, t_*, P_i) can be tuned at will to generate different enhancement patterns; as an example, and given that the timeframe of full enhancement of the fibroglandular tissue is usually in the order of one or few minutes,[34] in this work we set S_1 to 100 (dimensionless number), t_* to 60 s, and we present an example for P_i equal to both 1/0 and to 0.6/0.4.

The whole process described so far is repeated for each voxel in the breast in the original 3D breast CT image, resulting in a 4D image of time-varying iodine concentration in each voxel (a continuous amount), in addition to the 3D classified breast tissue type image (with each voxel value being a discrete value labeling the voxel as either skin tissue, adipose tissue, fibroglandular tissue, or vasculature).

2.E. Breast tumor models

After defining the enhancement dynamics of normal breast tissues, a tumor model can be added within the fibroglandular tissue of the breast. For this, the respective segmented mask is updated by defining a new voxel value for the tumor in the corresponding position.

Simulation of realistic lesions in breast computer phantoms has already been pursued by some investigators. Some used simple shapes (spherical or cylindrical), while others used 3-D random walk algorithms to simulate abnormalities, using logical operators,[35] primitive shapes,[36] and stochastic growth[37] to model benign and malignant masses.

In our work, to reproduce an accurate lesion model while keeping our phantom completely patient-based, we used a real tumor extracted from a breast CT patient scan. The tumor was segmented using a semi-automatic 3D level set.[38] For this, we manually defined the initialization of the level set within the breast mass, and we visually assessed the result (shown in Fig. 4). When generating the phantom, the user can select where to locate the lesion within the breast tissue, and set its desired size as a percentage of its original dimension (in this work, we used the original tumor dimensions as reported in Fig. 4).

Of course, breast tumors are characterized by usually having a different enhancement process than that of the surrounding healthy tissues, due to the large amount of small and often irregular newly formed vasculature. Furthermore, different tumor types show different enhancement patterns (according to malignancy grade and cellular type), resulting in a high intra-class variability.[39] For these reasons, additional steps are needed to better define different models of breast lesions within the proposed 4D phantom. To address this task, further parameters (besides the BV and BF) can be defined to model the contrast medium uptake of the lesion: the time to peak (i.e., the temporal moment corresponding to the highest enhancement of the lesion) and the wash-in and wash-out rates (i.e., the increase and decrease in the signal resulting from the in- and out-flow of the contrast medium
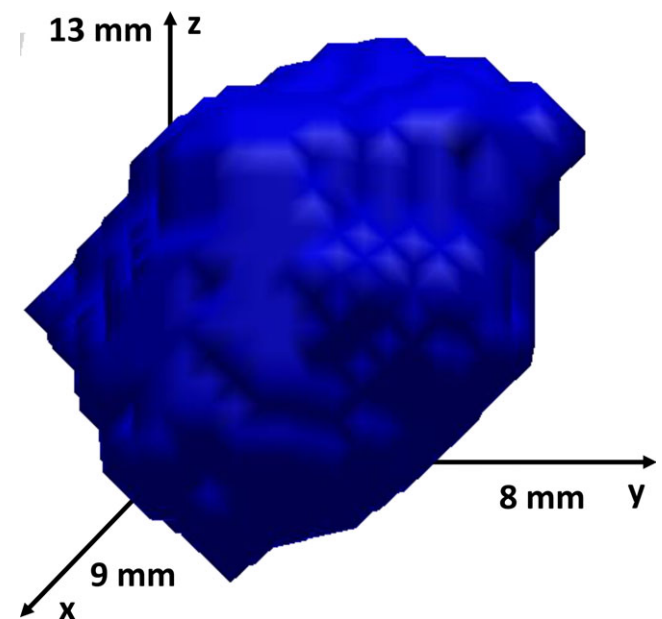

FIG. 4. Tumor model segmented from a patient breast CT scan and used in the present work. [Color figure can be viewed at wileyonlinelibrary.com]

within the tumor). These parameters are taken into account in the computation of the TEC for the tumor voxels by adding two computation steps after the convolution operation with the AIF: a temporal shift of the curve to the time to peak value, and a further final convolution with a polynomial function defined according to the selected wash-in and wash-out rates. This final operation is performed separately for the wash-in and wash-out phase (i.e., before and after the highest enhancement), allowing for the selection of different polynomial grades for the in- and out-flow, according to the following equation:

$$TEC_{tumor}(x, y, z, t) =$$
$$\begin{cases} TEC(x,y,z,t-t_{peak}) * R_{washin} & if\ t < t_{peak} \\ TEC(x,y,z,t-t_{peak}) * R_{washout} & if\ t > t_{peak} \end{cases} \quad (7)$$

In this work, two lesion models (benign and malignant) are generated by setting two different sets of tumor perfusion parameters (Table II).

To allow for a more varied breast lesion enhancement modeling, we added the possibility to simulate rim enhancement as an alternative to the uniform enhancement described above. Rim enhancement, more frequently seen in malignant breast lesions,[40] is characterized by a higher contrast medium uptake at the outer boundaries of the tumor, while the innermost portion remains almost unenhanced due to necrosis.[40] To simulate this effect, the 3D inverse distance transform[41] of the tumor is calculated and normalized between 0 and 1. This operation results in a 3D map labeling each voxel of the tumor with the distance from its center. This map is then multiplied by the following gaussian function, also normalized between 0 and 1:

$$R = \frac{1}{2\pi S_2^2} e^{\frac{-[x^2+y^2+z^2]}{2S_2^2}} \quad (8)$$

where x, y and z are the tumor voxels coordinates and S_2 the scale of the filter, which can be set at will. By multiplying this gaussian function with the inverse distance map, its radial distribution of voxel intensities gets stretched or shrunk according to the value of S_2, allowing for the simulation of the desired magnitude of the rim effect. Once the final 3D map is obtained, it is multiplied on a voxel-by-voxel basis with the time-enhancement curves of the tumor, selectively modifying them according to the distance from the tumor boundaries. As with all other parameters described in this work, the value of S_2 can be set at will (the higher the value, the lower is the rim effect, and therefore the more homogeneous the enhancement); as an example, in this study we applied the rim effect to the malignant lesion with a value for S_2 of 1,000 (dimensionless number).

3. RESULTS

As an example of the results of the algorithm, we describe two realizations of the 4D breast phantom, based on the same patient image acquired at our institution according to the process in Section 2.A; one with a malignant lesion and the

other with a benign lesion. A single frame of these 4D voxel breast phantoms has dimensions of $426 \times 421 \times 260$ (x, y, z), covering a volume of approximately $12 \times 12 \times 7$ cm; the temporal resolution (sampling time) can be defined at will. Both lesion models were located at the same coordinates within the fibroglandular tissue.

Figure 5 displays the shifted exponential functions (derived from the input perfusion parameters) used to calculate the TECs for the two tumor models and for the fibroglandular tissue.

Results of the generated phantoms show the expected enhancement of fibroglandular tissue and of the two breast lesions according to the given input parameters. Figure 6 shows four frames of the phantom for different temporal moments (t = 1 s, t = 120 s, t = 240 s, t = 510 s), while Fig. 7 displays the values of the TECs, averaged over the entire tumor volume, of the phantom with the malignant, homogeneous breast model (whose perfusion parameters are reported in Table II) generated with six different sampling times ($\Delta t = 1$ s, $\Delta t = 10$ s, $\Delta t = 20$ s, $\Delta t = 30$ s, $\Delta t = 60$ s, $\Delta t = 90$ s). As expected, lowering the temporal resolution decreases the amount of information which can be extracted from the 4D phantom; for the malignant tumor model, a temporal resolution lower than 90 s does not allow to depict any tumor enhancement.

Figure 8 shows the fibroglandular tissue and malignant lesion enhancements patterns for eight different frames of the 4D phantom (t = 1 s, t = 80 s, t = 120 s, t = 160 s, t = 180 s, t = 240 s, t = 300 s, t = 550 s), while Fig. 9 displays a magnification of the 120 s frame. As shown in Figs. 9(b) and 9(c), intra-tissue type biological variability is included in the developed phantom; therefore, voxels belonging to the same tissue type (in this case, the malignant tumor model) do not enhance exactly simultaneously and to the same maximum intensity.
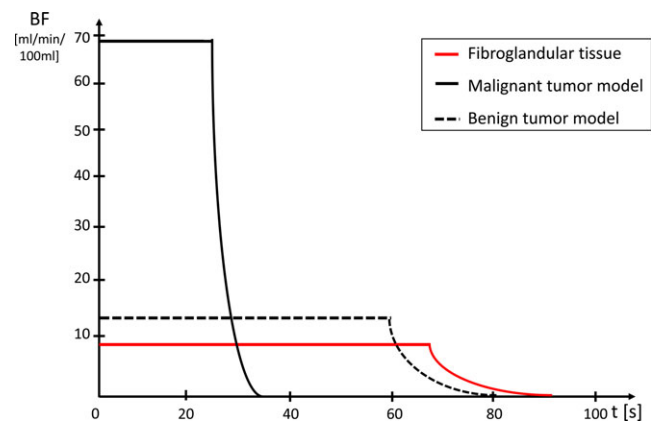

FIG. 5. Shifted exponential functions, which describe the perfusion parameters for a given tissue by modeling the fraction of contrast medium inside each tissue. The constant part of each curve models the perfusion of the tissue, while the exponential part the wash-out of contrast medium. The y-axis reports the flow of blood plus iodinated solution for a given tissue type. The concentration of the contrast medium within the blood, after the mean transit time, decreases exponentially during the wash-out phase, as modeled by the curves. [Color figure can be viewed at wileyonlinelibrary.com]
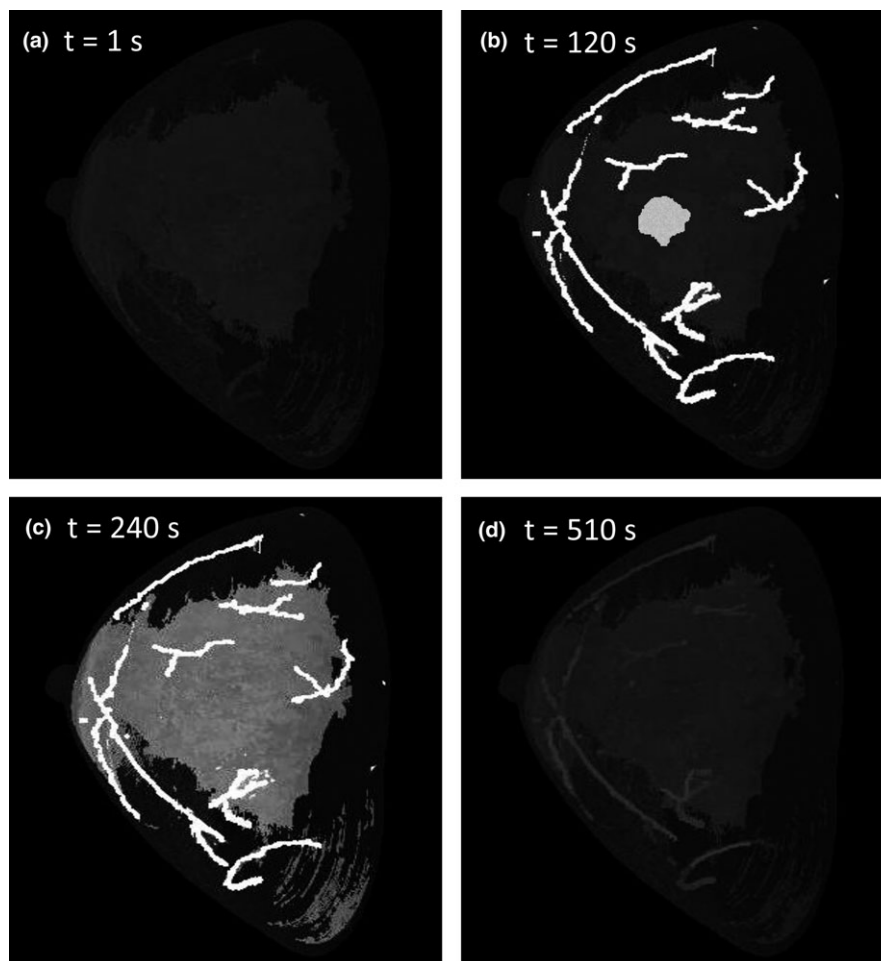
F<small>IG</small>. 6. Four 3D frames of the generated 4D voxel phantom with the malignant tumor model, for (a) 1 s, (b) 120 s, (c) 240 s, and (d) 510 s after injection. Each panel shows a single three-dimensional frame of the phantom, where each frame was obtained by projecting the voxel values of the phantom onto a projection plane. To allow a better visualization of more inner structures (e.g., the fibroglandular tissue and the tumor model), each point in the projection plane is assigned with the mean value of all voxels encountered.

Figure 10 shows a comparison between the two tumor models, displaying five frames from the two phantoms (t = 1 s, t = 120 s, t = 240 s, t = 300 s, t = 380 s) and their respective time enhancement curves. As expected, the two breast lesion models show different enhancement dynamics; the malignant tumor model presents a high and fast enhancement, with high wash-in and wash-out rates, while the benign one shows a lower enhancement and more gentle wash-in and wash-out degree, simulating a lower contrast medium uptake due to a smaller perfusion rate.

Figure 11 displays two examples of the enhancement pattern of the breast fibroglandular tissue within the phantom according to the distance from the two arterial input sources.

Finally, Fig. 12 shows the malignant tumor model within the phantom for three temporal moments, generated both with homogeneous and with rim enhancement.

The computational time needed by the algorithm to generate a complete 4D phantom varies according to the number of breast voxels in the input images. As an example, for an average breast size with reconstructed voxel dimensions of 0.273 mm a side, the algorithm takes approximately 5 min per slice for a full acquisition time range of 560 s and a temporal resolution of 1 s. The computational time decreases approximately by a factor of $\Delta t^{0.7}$, where Δt is the desired temporal resolution (the algorithm was developed in Matlab and run on a 2.7 GHz CPU, 8 GB RAM workstation).

4. DISCUSSION

Generating breast phantoms for research purposes has been pursued by a number of investigators and presents many challenges. Physical phantoms are not completely adjustable, usually do not result in a completely known independent truth, and do not realistically mimic the complexity of breast anatomy, but can be used on real imaging systems, avoiding simulations and their necessary, even if minor, simplifying assumptions. Digital phantoms, on the other hand, can offer improved realism, are fully adjustable, and allow for knowledge of the ground truth, but of course cannot be used for real imaging. Consequently, the primary benefit of using digital phantoms is the ability to simulate and control many aspects of the imaging process, so that the behavior of an algorithm or a simulated imaging system can be carefully optimized and/or evaluated with the important advantage that the
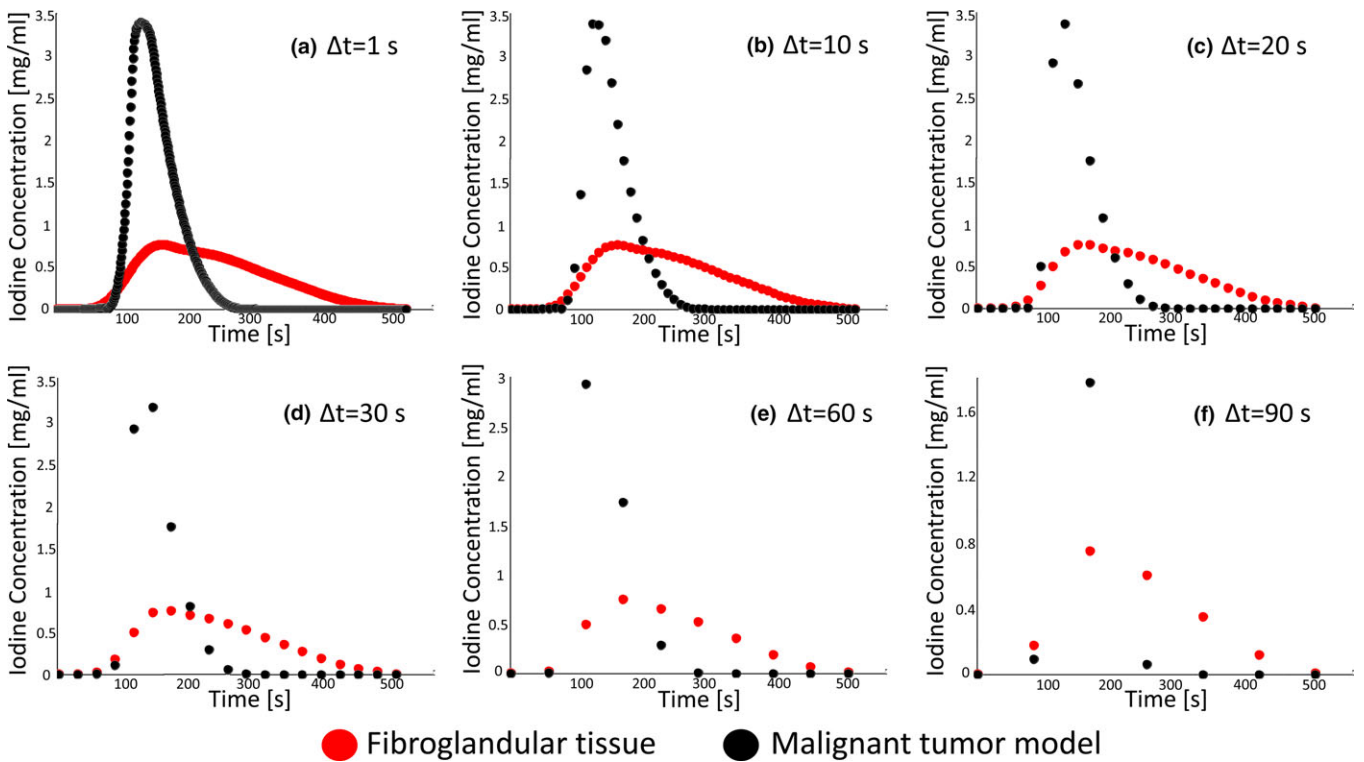
FIG. 7. Average time enhancement curves (TECs) of the phantom with the malignant, homogeneous breast model generated with six different sampling times: (a) 1 s, (b) 10 s, (c) 20 s, (d) 30 s, (e) 60 s, (f) 90 s. [Color figure can be viewed at wileyonlinelibrary.com]
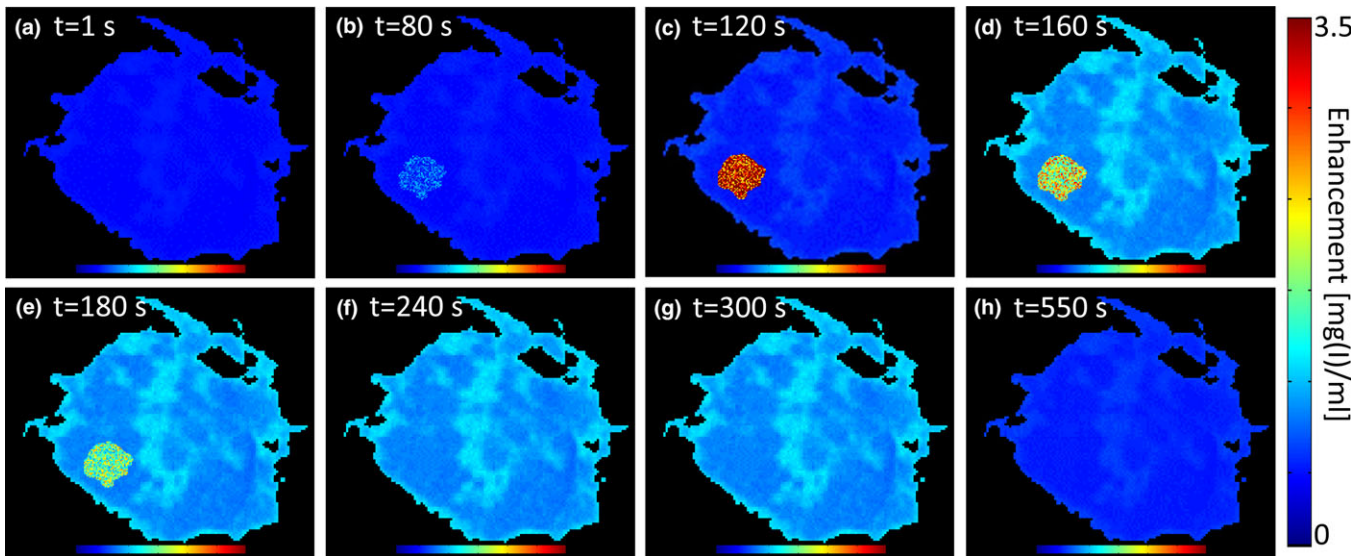

FIG. 8. Portion of the breast phantom showing the fibroglandular tissue and malignant lesion enhancement patterns for eight different frames (one slice each) from the 4D phantom after different times: (a) 1 s, (b) 80 s, (c) 120 s, (d) 160 s, (e) 180 s, (f) 240 s, (g) 300 s, (h) 550 s. [Color figure can be viewed at wileyon linelibrary.com]

ground truth is known *a priori*. Furthermore, unlike physical phantoms, modifications such as identifying particular structures, adding pathologies, and highlighting activation areas are easily performed.

The proposed pipeline can be used to generate multiple 4D phantoms from patient cases and with different tumor models, spanning the clinical range of breast sizes, glandular fractions, and pathological conditions. Moreover, by having full control of several input parameters (e.g., iodine concentration, acquisition time range, perfusion parameters, and patterns) a wide range of conditions can be simulated, resulting in a range of possible variations in the input iodine concentration, the resulting image contrast and the enhancement patterns for different tissues and lesions.
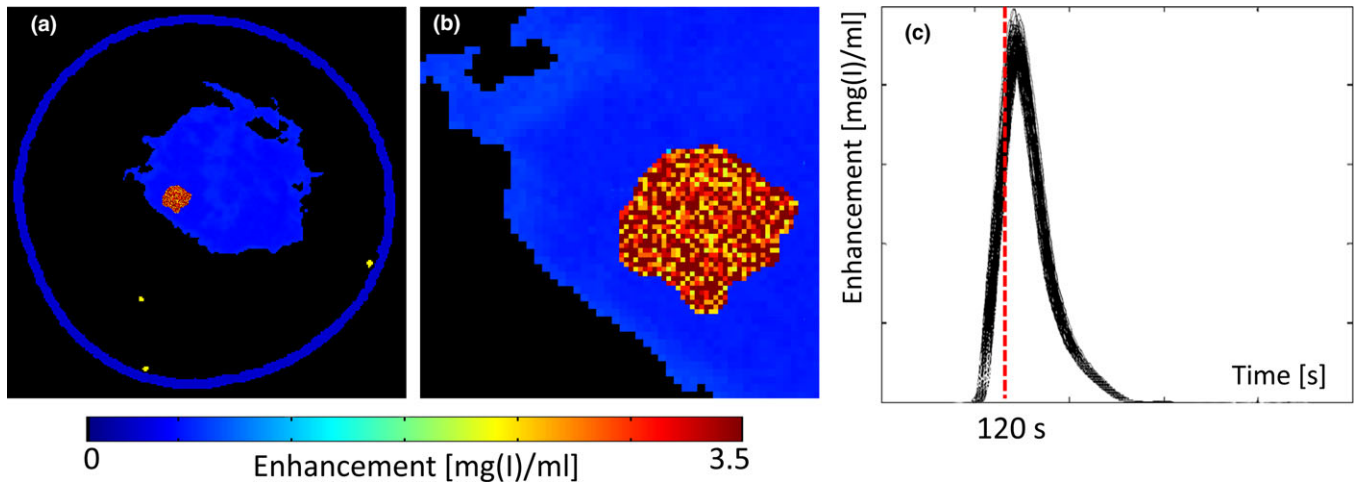
FIG. 9. (a) One slice from the 120 s frame of the 4D phantom containing the malignant tumor model; (b) its magnification, and (c) the respective time enhancement curves of the tumor voxels. [Color figure can be viewed at wileyonlinelibrary.com]
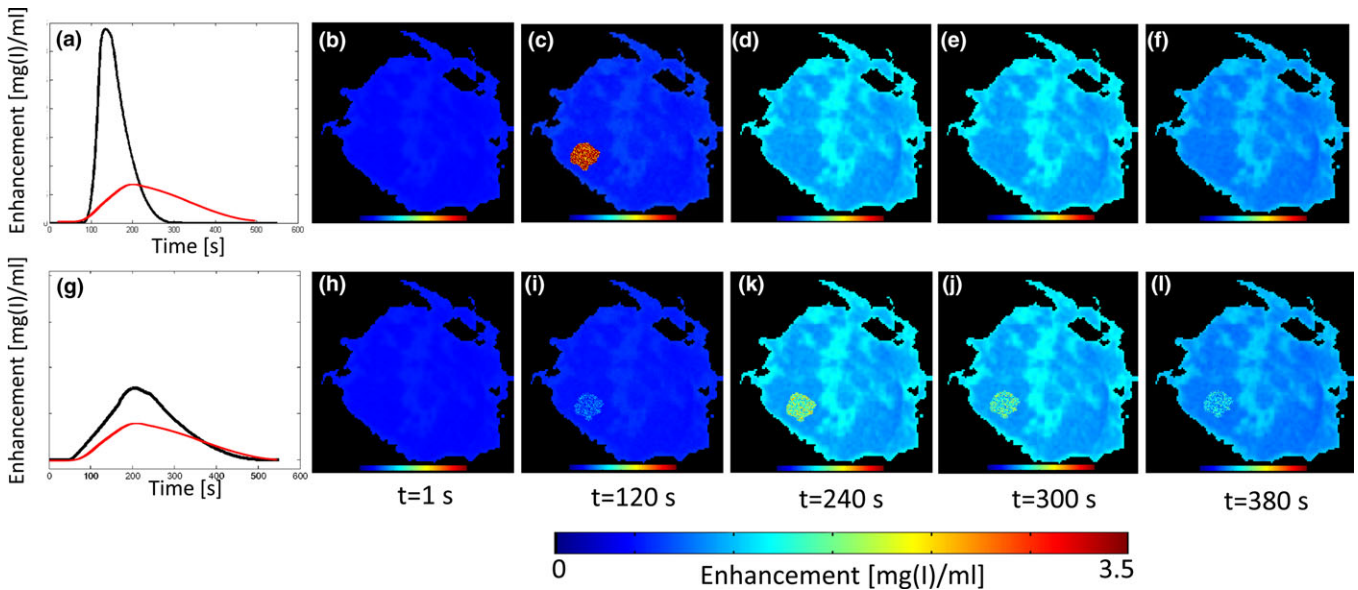

FIG. 10. Five frames (one slice each) showing a portion of the 4D phantom with the (top row) malignant and (bottom row) benign tumor model, for different times after injection: (b, h) 1 s, (c, i) 120 s, (d, j) 240 s, (e, k) 300 s, (f, l) 380 s. Panels (a) and (b) show the average time enhancement curves for both cases. [Color figure can be viewed at wileyonlinelibrary.com]

4D virtual breast phantoms have been proposed previously.[42] These phantoms were developed by incorporating contrast agent propagation kinetics into the extended cardiac torso (XCAT) breast phantoms. The perfusion parameters, as well as the temporal parameters modeling the enhancement, were estimated based on the relative vascularization of various tissues with the same trends reported in previous MRI studies.[27] These phantoms, which were used to simulate and optimize both mammographic and digital breast tomosynthesis imaging systems, model the 4D aspect as the fraction of tissue material in the effective tissue-contrast agent-blood mixture. Although useful in phantom-based simulations, these phantoms do not take into account many physiological or pathological aspects which may be found in a real breast (e.g., different enhancement kinetics for breast lesions,

biological variability, different parenchyma enhancement patterns). Our approach allows for varying several input parameters, covering a wide scenario of physiological and pathological conditions, and therefore allowing for more realistic simulations of dynamic breast imaging systems.

All parameters involved in the generation of the phantom can be defined at will. Within this study and as a matter of example, the fractions used for different materials in the breast were estimated based on the relative vascularization of various tissues detected using MRI.[27] Although the contrast uptake measurements within the breast may provide different results between gadolinium and iodine, this approach has been followed in previous studies which propose CT-based phantoms or simulations,[21,42] due to the extensive evaluation of breast functional studies previously performed using MRI.
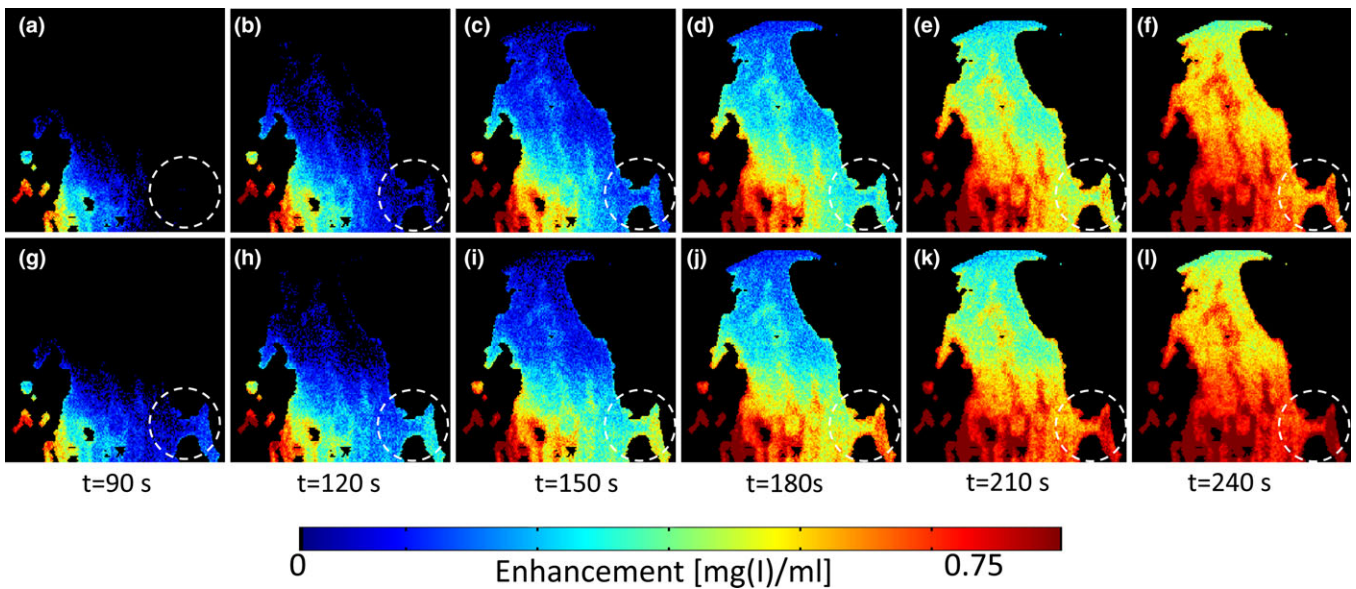
FIG. 11. Example of the phantom (axial view) fibroglandular tissue with the background parenchyma enhancement varying according to the distance from the two source locations modeling the arterial supply. Top panel (a–f) shows the phantom generated with P_i equal to 1/0, while bottom panel (g–l) with P_i equal to 0.6/0.4. In both examples, the parameters which model the enhancement were set to 100 (S_1), 60 s (t_*). [Color figure can be viewed at wileyonlinelibrary.com]
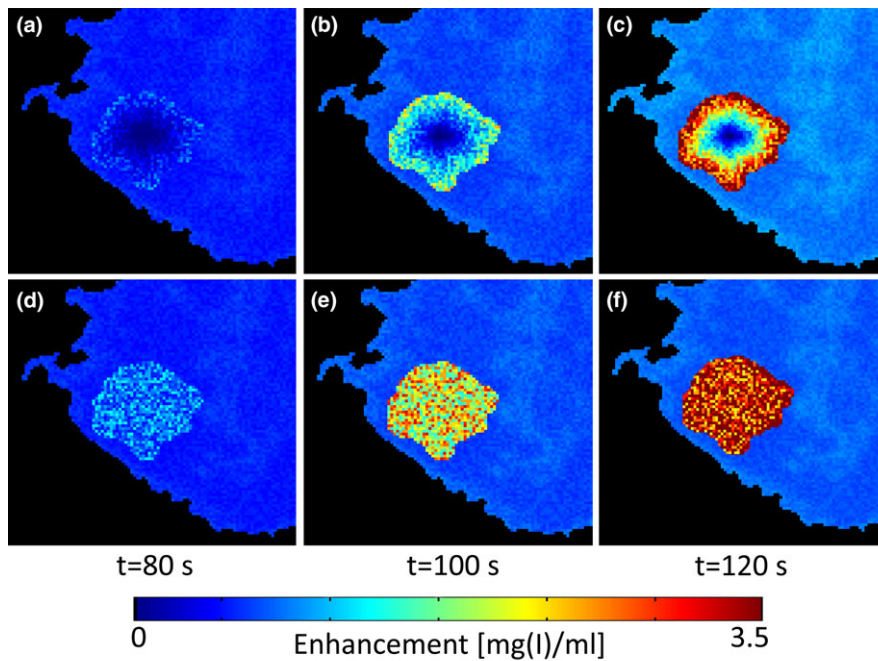

FIG. 12. Malignant tumor model within the phantom for three temporal moments, generated both with rim (top panel) and with homogeneous enhancement (bottom panel). [Color figure can be viewed at wileyonlinelibrary.com]

The temporal resolution (i.e., the sampling time) of the proposed phantoms can be modified at will, allowing to simulate different image acquisition settings. Moreover, modifying the sampling time and evaluating different lesion types within the phantom could be useful to assess the impact of the finite temporal resolution of the breast CT system and its impact on the ability to obtain accurate information on the enhancement process in breast tumors, which could be useful for diagnosis and staging.

Beside the temporal resolution and all other input parameters, further evaluation of other aspects of image acquisition might also be evaluated with the proposed phantom. In light of this, future work will include the simulation of the entire DCE-breast CT imaging chain, including raytracing and Monte Carlo simulations for x ray scatter and radiation dose estimates.

Especially, our methods allow for the generation of dynamic 4D phantoms, modeling the contrast medium uptake

dynamics across the different breast tissues starting from a single, static, unenhanced 3D breast CT image as input. In addition to the static anatomical information, each phantom voxel represents the iodine content at that location at a given moment in time, therefore, allowing for the simulation of dynamic breast CT imaging. Since all physical parameters of all materials within the phantom are known, patient-based dynamic computer simulations of DCE-breast CT imaging (e.g., involving Monte Carlo methods) will be able to be performed. With these simulations, time-varying projection images of the phantom can be generated given a wide range of acquisition settings, allowing for the optimization of DCE-breast CT imaging in terms of acquisition technique, dose level, temporal sampling requirements, etc. This would allow for the design and optimization of a DCE-breast CT starting from noncontrast patient images acquired using a static breast CT system.

The proposed method can also be used to optimize and validate methods for quantitative perfusion studies of breast lesions obtained with DCE-breast CT. In fact, by generating multiple phantoms with different lesion types, dedicated image analysis techniques for cancer development risk assessment, tumor type characterization, and treatment response evaluation, could be validated, albeit this is dependent on the available knowledge on biological processes that affect lesion enhancement.

The phantoms derived from the methods we propose have some limitations. First, being generated from real 3D patient breast CT images, the spatial resolution of the phantom is limited by the characteristics of the breast CT system used to scan the patient breasts. This leads to representing a continuous object (the breast) with a discrete model (the phantom), possibly leading to inaccuracies for subsequent phantom-based simulations. In future work, we will evaluate different methods to increase the resolution of our phantoms to improve their realism. Second, the current implementation does not include any breast tissue motion due to respiration or blood pulsation. Finally, only one tumor model (although showing different enhancement patterns) was included in this study. In the future, a larger dataset of lesion models may be generated from direct segmentation from other patient images. Beside the lesions shape, further different perfusion parameters and different enhancement patterns within the same tumor could also be tested and evaluated.

5. CONCLUSIONS

The digital phantoms deriving from the method we propose can model the behavior of contrast in the breast during DCE-breast CT image acquisition, displaying the different enhancement dynamics that may be found in a patient breast. Multiple phantoms from patient cases with different tumor models can be generated at will. These phantoms will be used to optimize the development of dynamic contrast-enhanced dedicated breast CT imaging, especially in image acquisition simulations, and the

validation of quantitative image analysis algorithms that will be used to calculate the time enhancement curves, and therefore characterize the perfusion in real patient images. Future work includes the evaluation of the enhancement of different tumor types and the simulation of the DCE-breast CT imaging chain.

CONFLICTS OF INTEREST

The authors have no relevant conflicts of interest to disclose.

a)Author to whom correspondence should be addressed. Electronic mail: ioannis.sechopoulos@radboudumc.nl.

REFERENCES

1. Ferlay J, Steliarova-Foucher E, Lortet-Tieulent J, et al. Cancer incidence and mortality patterns in Europe: estimates for 40 countries in 2012. *Eur J Cancer*. 2013;49:1374–1403.
2. Paci E, Broeders M, Hofvind S, Puliti D, Duffy SW. European breast cancer service screening outcomes: a first balance sheet of the benefits and harms. *Cancer Epidemiol Biomarkers Prev*. 2014;23:1159–1163.
3. Ferlay J, Soerjomataram I, Dikshit R, et al. Cancer incidence and mortality worldwide: sources, methods and major patterns in GLOBOCAN 2012. *Int J Cancer*. 2015;136:E359–E386.
4. Feng SSJ, Sechopoulos I. Clinical digital breast tomosynthesis system: dosimetric characterization. *Radiology*. 2012;263:35–42.
5. Hofvind S, Hovda T, Holen AS, et al. Digital breast tomosynthesis and synthetic 2D mammography versus digital mammography: evaluation in a population-based screening program. *Radiology*. 2018;287:787–793.
6. Sechopoulos I, Feng SSJ, D'Orsi CJ. Dosimetric characterization of a dedicated breast computed tomography clinical prototype. *Med Phys*. 2010;37:4110–4120.
7. Turnbull LW. Dynamic contrast-enhanced MRI in the diagnosis and management of breast cancer. *NMR Biomed*. 2009;22:28–39.
8. Prionas ND, Lindfors KK, Ray S, et al. Contrast-enhanced dedicated breast CT: initial clinical experience. *Radiology*. 2010;256:714–723.
9. Wienbeck S, Fischer U, Luftner-Nagel S, Lotz J, Uhlig J. Contrast-enhanced cone-beam breast-CT (CBBCT): clinical performance compared to mammography and MRI. *Eur Radiol*. 2018;28:3731–3741.
10. Uhlig J, Fischer U, Von Fintel E, et al. Contrast-enhancement on cone-beam breast CT for discrimination of breast cancer immunohistochemical subtypes. *Translat Oncol*. 2017;10:904–910.
11. Perrone A, Lo Mele L, Sassi S, et al. MDCT of the breast. *AJR Am J Roentgenol*. 2008;190:1644–1651.
12. Cuenod CA, Fournier L, Balvay D, Guinebretière JM. Tumor angiogenesis: pathophysiology and implications for contrast-enhanced MRI and CT assessment. *Abdom Imaging*. 2006;31:188–193.
13. Goh V, Padhani AR. Imaging tumor angiogenesis: functional assessment using MDCT or MRI? *Abdom Imaging*. 2006;31:194–199.
14. Driscoll B, Keller H, Coolens C. Development of a dynamic flow imaging phantom for dynamic contrast-enhanced CT. *Med Phys*. 2011;38:4866–4880.

15. Prionas ND, Burkett GW, McKenney SE, Chen L, Stern RL, Boone JM. Development of a patient-specific two-compartment anthropomorphic breast phantom. *Phys Med Biol*. 2012;57:4293–4307.

16. Schindera ST, Nelson RC, Mukundan S. Hypervascular liver tumors: low tube voltage, high tube current multi-detector row CT for enhanced detection-phantom study. *Radiology*. 2008;246:125–132.

17. Wood RP, Khobragade P, Ying L, et al. Initial testing of a 3D printed perfusion phantom using digital subtraction angiography. *Proc SPIE Int Soc Opt Eng*. 2015;9417:94170V-1:11.

18. Haberland U, Cordes J, Lell M, Abolmaali N, Klotz E. A biological phantom for contrast-media-based perfusion studies with CT. *Invest Radiol*. 2009;44:676–682.

19. Collins DL, Zijdenbos AP, Kollokian V, et al. Design and construction of a realistic digital brain phantom. *IEEE Trans Med Imaging*. 1998;17: 463–468.

20. Hoeschen C, Fill U, Zankl M, Panzer W, Regulla D, Dohring W. A high-resolution voxel phantom of the breast for dose calculations in mammography. *Radiat Protect Dos*. 2005;114:406–409.

21. Riordan AJ, Prokop M, Viergever MA, Dankbaar JW, Smit EJ, De Jong HWAM. Validation of CT brain perfusion methods using a realistic dynamic head phantom. *Med Phys*. 2011;38:3212–3221.

22. Han MC, Seo JM, Lee SH, et al. Continuously deforming 4D voxel phantom for realistic representation of respiratory motion in Monte Carlo dose calculation. *IEEE Trans Nucl Sci*. 2016;63:2918–2924.

23. O'Connell A, Conover DL, Zhang Y, et al. Cone-beam CT for breast imaging: radiation dose, breast coverage, and image quality. *AJR*. 2010;195:496–509.

24. Boone JM, Nelson TR, Lindfors KK, Seibert JA. Dedicated breast CT: radiation dose and image quality evaluation. *Radiology*. 2001;221:657–667.

25. Caballo M, Boone JM, Mann R, Sechopoulos I. An unsupervised automatic segmentation algorithm for breast tissue classification of dedicated breast computed tomography images. *Med Phys*. 2018;45:2542–2559.

26. Cuenod CA, Balvay D. Perfusion and vascular permeability: basic concepts and measurement in DCE-CT and DCE-MRI. *Diagn Intervent Imaging*. 2013;94:1187–1204.

27. Delille JP, Slanetz PJ, Yeh ED, Kopans DB, Garrido L. Breast cancer: regional blood flow and blood volume measured with magnetic susceptibility–based MR imaging—initial results. *Radiology*. 2002;223:558–565.

28. Woolf DK, Taylor NJ, Makris A, et al. Arterial input functions in dynamic contrast-enhanced magnetic resonance imaging: which model performs best when assessing breast cancer response? *Br J Radiol*. 2016;89:20150961.

29. George RT, Ichihara T, Lima JAC, Lardo AC. A method for reconstructing the arterial input function during helical ct: implications for myocardial perfusion distribution imaging. *Radiology*. 2010;255:396–403.

30. Han S. A quantification method for breast tissue thickness and iodine concentration using photon-counting detector. *J Digit Imaging*. 2015; 28:594–603.

31. Zierler KL. Theoretical basis of indicator-dilution methods for measuring flow and volume. *Circ Res*. 1962;10:393–407.

32. King V, Brooks JD, Bernstein JL, Reiner AS, Pike MC, Morris EA. Background parenchymal enhancement at breast MR imaging and breast cancer risk. *Radiology*. 2011;260:50–60.

33. Kaiser WA. *Signs in MR Mammography*. Berlin: Springer; 2008.

34. Van der Velden BHM, Sutton EJ, Carbonaro LA, Pijnappel RM, Morris EA, Gilhuijs KGA. Contralateral parenchymal enhancement on dynamic contrast-enhanced MRI reproduces as a biomarker of survival in ER-positive/HER2-negative breast cancer patients. *Eur Radiol*. 2018. https://doi.org/(10.1007/s00330-018-5470-7)

35. Zhou L, Oldan J, Fisher P, Gindi G. Low-contrast lesion detection in tomosynthetic breast imaging using a realistic breast phantom. Proc. SPIE 6142, Medical Imaging 2006: Physics of Medical Imaging, 61425A.

36. Bliznakova K, Bliznakov Z, Bravou V, Kolitsi Z, Pallikarakis N. A three-dimensional breast software phantom for mammography simulation. *Phys Med Biol*. 2003;48:3699–3719.

37. Gong X, Glick SJ, Liu B, Vedula AA, Thacker S. A computer simulation study comparing lesion detection accuracy with digital mammography, breast tomosynthesis, and cone-beam CT breast imaging. *Med Phys*. 2006;33:1041–1052.

38. Chan TF, Vese LA. Active contours without edges. *IEEE Trans Im Proc*. 2001;10:266–276.

39. Folkman J. What is the evidence that tumors are angiogenesis dependent? *J Natl Cancer Inst*. 1990;82:4–6.

40. Liberman L, Morris EA, Lee MJ, et al. Breast lesions detected on MR imaging: features and positive predictive value. *AJR Am J Roentgenol*. 2002;179:171–178.

41. Kimmel R, Kiryati N, Bruckstein AM. Distance maps and weighted distance transforms. *J Math Imaging Vis*. 1996;6:223–233.

42. Kiarashi N, Lo JY, Lin Y, et al. Development and application of a suite of 4-D virtual breast phantoms for optimization and evaluation of breast imaging systems. *IEEE Trans Med Imaging*. 2014;33:1401–1409.